Stand-off Thermal IR Minefield Survey: System concept and experimental results

Frank Cremer[1], Thành Trung Nguyen[2], Lixin Yang[2], and Hichem Sahli[1,2]
[1]Interuniversity Micro Electronics Centre, ETRO Department, Pleinlaan 2, B1050 Brussels, Belgium
[2]Vrije Universiteit Brussel, ETRO Department, Pleinlaan 2, B1050 Brussels, Belgium

ABSTRACT

A detailed description of the CLEARFAST system for thermal IR stand-off minefield survey is given. The system allows (i) a stand-off diurnal observation of hazardous area, (ii) detecting anomalies, i.e. locating and searching for targets which are thermally and spectrally distinct from their surroundings, (iii) estimating the physical parameters, i.e. depth and thermal diffusivity, of the detected anomalies, and (iv) providing panoramic (mosaic) images indicating the locations of suspect objects and known markers. The CLEARFAST demonstrator has been successfully deployed and operated, in November 2004, in a real minefield within the United Nations Buffer Zone in Cyprus. The paper describes the main principles of the system and illustrates the processing chain on a set of real minefield images, together with qualitative and quantitative results.

Keywords: Thermal infrared, stand-off detection, area reduction, diurnal measurements.

1. INTRODUCTION

The use thermal infrared (IR) sensors for landmine detection have been of interest since the 1950s [1]. IR sensors allow the measurement of the surface temperature. For landmine detection, landmines are thought of as a thermal barrier in the natural flow of the heat inside the soil, which produces a perturbation of the expected thermal pattern on the surface. The detection of these perturbations (anomalies) will put into evidence the presence of potential landmine targets [2].

Most thermal detection system use single images (snapshots) to distinguish between undisturbed soil and soil above a landmine. These snapshots give limited information on the so-called anomalies and may be taken at a wrong time. During the course of a non-cloudy diurnal cycle (assuming the landmine blocks the heat flow) the soil above the landmine is warmer during the day and colder during night compared to undisturbed soil. This naturally implies that there are two times during the day where there is no difference in temperature. These so-called zero contrast periods occur around sunrise and sunset [2].

Performing anomaly detection on diurnal data prevents problems during the zero contrast periods. Furthermore, by modelling the behaviour of the anomalies and comparing with the actual behaviour, physical parameters such as depth and thermal diffusivity could be extracted. Comparing the thermal diffusivity with the diffusivity of the material of the expected landmines gives a very important cue for deciding the relevance of the anomaly [2]. This paper presents the use of thermal IR sensor under changing natural illumination and environmental conditions, and the subsequent image analysis to produce appropriate information to facilitate the identification of buried targets. Thermal modelling for the identification of landmines is extensively described in another paper in these proceedings [3].

The paper is organised as follows. Section 2, gives an overview of the CLEARFAST concept and its deployment. Section 3 deals with the data pre-processing step. In Section 4, a mathematical morphology-based approach for anomaly detection is given. Section 5 describes the mosaic generation of the surveyed area, depicting the location of suspected targets. In Section 6 the system deployment on a real minefield and the obtained results are described. Finally discussion and conclusion are given in Section 7.

Email addresses: {fcremer, ntthanh, lxyang, hsahli}@etro.vub.ac.be

2. CLEARFAST SYSTEM CONCEPT

2.1. System Description

The CLEARFAST survey concept is based on a stand-off observation covering larger area then the field of view of the thermal IR camera. Figure 1 shows how the system could be deployed, and the demonstrator components: (a) Survey Platform, (b) Auxiliary Data Station, and (c) Control Station.

a) As survey platform a telescopic boom lift has been selected (Mateco Boom lift type T 157 KD 4x4B). The payload mounting as well as the Data Acquisition Unit is placed on the sky-lift platform. The payload mounting corresponds to an aluminium frame mounted on the platform of the jib. The aluminium frame can be tilted from 0 to 90 degrees off normal.
The payload consists of two sub-units: (1) an outer gimbal envelope, the turret, mounted on a carrying platform, and acting as pan device, and (2) a plug-in sensor module. The sensor module, including a Multi-spectral IR (MSIR) camera and visible camera, slides into the turret gimbal, acting as sensor slice and as inner gimbal (Tilt device). All the connector's and cables are attached to the carrying platform. This modular approach allows an easy maintenance in case of failure: the sensor 'slice' can be replaced without removing the payload from the platform.
In order to record the position of survey platform, and achieve the desired accuracy within a few centimetres, a DGPS System, operating in RTK (Real Time Kinematics) mode is used.

b) Auxiliary Data Station: Besides the images of the multi-spectral IR and visible cameras, additional data is necessary for thermal model parameter estimation and image analysis. This data consists of meteorological data (weather station) and soil temperature measurements. The weather station is an additional measurement instrument providing: air temperature, humidity, wind speed, air pressure, solar irradiation, precipitation and sky radiance. The system, connected to the Image Processing workstation, is acquiring data once every minute. Furthermore the temperature of the soil, at different depths, is important for both the thermal modelling and image analysis (where only the surface temperature is important). Thermocouple with automatic temperature logging devices instruments is used, and connected to the Image Processing Workstation.

c) The control station consists of two workstations: (1) a Data Acquisition Control Unit enabling the control of the line of sight of the cameras (scanning), the data acquisition and storage, and (2) an Image Processing Workstation dealing with the data processing. The image processing details are given in Sections 3 to 5.

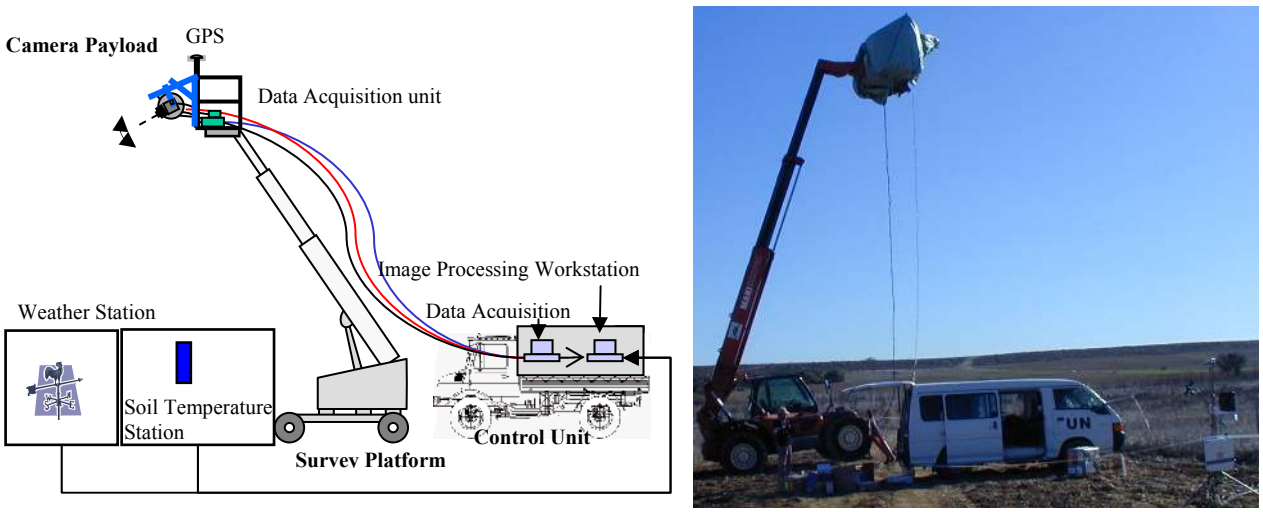

Figure 1: The CLEARFAST system concept and its deployment at a minefield in Cyprus.

2.2. Survey Characteristics

Following the CLEARFAST concept for surveying a large area with a spatial/thermal resolution that is high enough allowing the detection of shallowly buried mines, a tool has been designed allowing the setting-up of a scanning mission (pattern). The scanning mission takes into account the main parameters for a good survey in terms of image analysis, namely (a) number of images, (b) the pixel resolution in elevation (depth) and azimuth (width), and (c) number of diurnal images (i.e. number of scans and delay between scans). These parameters are estimated according to the platform height, the camera field of view (FOV), and the area coverage. In order to reduce the image blurring, due to the filter wheel, the scanning is performed in stop-and-go mode: i.e. move the pan/tilt, still position, acquire a set of MSIR images. Figure 6 shows a mosaic of an area of 20m x 30m obtained following a scanning pattern of 261 positions (images).

3. PRE-PROCESSING STEPS

An overview of the CLEARFAST pre-processing chain is given in Figure 2. The first step is the radiometric calibration that uses the temperature readouts T_1 and T_2 from the blackbodies (section 3.3). Once the radiometric calibration is performed, the different thermal spectral bands are co-registered. In order to provide correspondence in time, the images are temporally co-registered (section 3.4). A correction is performed for atmospheric attenuation and emission, using the air temperature T_{air}, the relative humidity (RH) and the air pressure (section 3.5). Finally the images are converted into apparent temperatures (section 3.6).

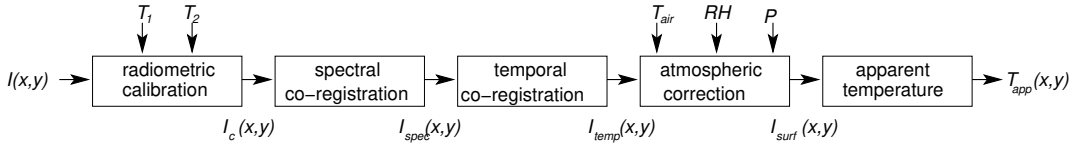

Figure 2: Overview of the CLEARFAST pre-processing steps.

3.3. Radiometric calibration

This procedure provides the radiometric calibrated images [4][5], after which the image grey values are provided in physical units: $W/m^2/sr$. The calibration is valid under the following assumptions:

- The blackbodies have a uniform temperature over their full surface.
- The blackbodies have an emission coefficient of 1.
- The temperature readout of the blackbodies is correct.
- The transmission losses between blackbody and the camera are negligible.
- The output of the camera (digital pixel values) has a linear relationship with the radiance for each pixel.

During image acquisition, the calibration procedure is shown in Figure 3 and outlined as follows:

1. The camera is oriented to the first blackbody. This blackbody is heated (around 10 K above ambient temperature).
2. A set of images (10 or more) are acquired of the first blackbody.
3. The camera is oriented at the second blackbody. This blackbody is not heated and is therefore at or near ambient temperature.
4. A set of images (10 or more) are acquired of the second blackbody.
5. The temperatures of the blackbodies are recorded every minute.
6. The camera is oriented at the scene and a set of images, corresponding to the scanning pattern, are acquired.

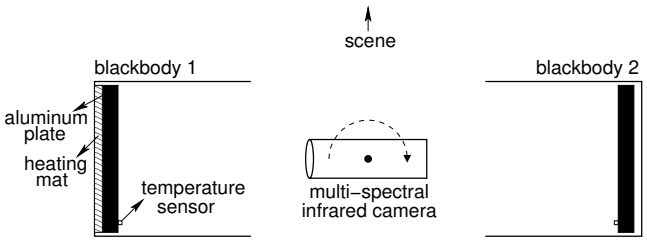

Figure 3: Calibration procedure using two blackbodies (one heated and one at ambient temperature) with temperature sensors and a camera on a pan/tilt unit.

The acquired images, *I(x, y)*, are calibrated using Eq.1, after a full scan of the area has been performed.

$$I_c(x,y) = I_{r1} + \frac{I(x,y) - I_{bb1}(x,y)}{I_{bb2}(x,y) - I_{bb1}(x,y)}\left(I_{r2} - I_{r1}\right) \qquad [\mathrm{W/m^2/sr}], \qquad (1)$$

with, $I_{bb1}(x, y)$ and $I_{bb2}(x, y)$ are average blackbody images, for blackbody #1 and #2, respectively. I_{ri} (i=1,2) are the blackbodies radiances, estimated using Planck's equation (Eq.2.):

$$I_{ri} = \int_{\lambda_1}^{\lambda_2} \frac{2hc^2}{\lambda^5} \frac{1}{e^{\frac{hc}{\lambda k T_i}} - 1} d\lambda \qquad [\mathrm{W/m^2/sr}], \qquad (2)$$

Where, T_i (i=1, 2) are the measured blackbodies temperatures; λ_1 and λ_2 are respectively the lower and upper bound of the wavelength of the MSIR camera. The integral in Eq.2 is numerically solved using the adaptive Simpson quadrature method [6].

The resulting image radiance, $I_c(x, y)$, is directly related to the radiance of the scene. All effects from the camera and filter are removed by performing this calibration regularly (for example every 15 minutes or between two full scans of the area). Opposite to radiance in the visual wavelength bands, the radiance in this wavelength band consists of two different components. The first component is comparable to the visual wavelength band and consists of the reflected radiance from the object, where the sun and the sky are the main sources 'illuminating' on the object. In the infrared wavelength bands, however, every object also has an emission of its own. The amount of emission depends on the temperature of the object and the surface properties (that determine the radiative effectiveness of the object).

Eq.1. has been given for a single pixel. However, we have assumed the blackbodies to be uniform over the full area. What are the implications if we perform this approach for the full image? In effect the linear mapping from digital values to calibrated radiance is performed independently for each pixel. This independence implies that if there are any differences between pixels in sensitivity and/or offset then these differences, called *non-uniformity*, are no longer present in the calibrated image. Opposed to visual cameras, differences in sensitivity and/or offset are quite common in infrared images. Therefore a non-uniformity correction is necessarily and often integrated in the camera. Nonetheless the calibration for the non-uniformity must be performed regularly, since the non-uniformity gradually changes with time, unless scene-based non-uniformity methods are performed [6]. For the multi-spectral infrared measurements, this non-uniformity correction is even more important. Due to difference in the optical path, reflections or the temperature distribution over the filter, there is a non-uniform distortion of the image on top of the non-uniformity of the detector array. By performing the aforementioned calibration both non-uniformities are resolved in a single step.

3.4. Temporal co-registration

As our concept deals with diurnal, and hence, time series analyses, it is necessary to correct for the misalignment of the images that is mainly due to the movement of the camera and/or platform during the diurnal acquisition. This is done via a temporal co-registration procedure.

The developed temporal co-registration is based on a parametric displacement model, namely, the linear conformal model (Eq.3.), implemented in an optimization framework.

$$(\boldsymbol{u},\boldsymbol{v}) = \begin{bmatrix} \boldsymbol{x} & \boldsymbol{y} & 1 \end{bmatrix} \begin{bmatrix} \cos\boldsymbol{\alpha} & -\sin\boldsymbol{\alpha} \\ \sin\boldsymbol{\alpha} & \cos\boldsymbol{\alpha} \\ \boldsymbol{tx} & \boldsymbol{ty} \end{bmatrix} \tag{3}$$

with (*tx*, *ty*) is the 2-D translation vector and α is the rotation angle.

The maximal Mutual Information (MI) is used as co-registration criterion (objective function). This approach allows taking into account contrast changes during diurnal observations. MI is a basic concept from information theory, a suitable similarity measure between two images, and has been widely used in many medical image applications and remote sensing images [7][8] for both Multi-temporal and multi-spectral image analysis. The MI registration criterion states that the MI of the image intensity values of corresponding pairs is maximal if the two images are geometrically aligned by a transformation.

3.5. Atmospheric correction

Due to the path between the camera and the scene the radiance from the objects is attenuated. Even though the path length is relatively small (around 20 m), the attenuation is not negligible (it is in the order of 10%). Complex atmospheric models have been built to estimate the attenuation and the path radiance. These models use the specific constitution of the atmosphere and the characteristics of the gas molecules to calculate the transmission and emission. Moreover, aside from the path length and the wavelength interval, several meteorological measurements are also used:

1. Air temperature (T_{air})
2. Relative Humidity (RH)
3. Air pressure (P)

For the atmospheric correction we use the MODTRAN [9] atmospheric model. It provides the transmission coefficient τ_a and the path radiance I_a. The radiance originating from the surface (I_{surf}), which is the one that we are interested in, is attenuated by τ_a due to absorption in the atmosphere, whereas the path radiance increases the measured radiance. The relationship between the calibrated radiance, I_c, and the surface radiance, I_{surf}, is given by:

$$I_c = \tau_a I_{surf} + I_a \qquad [\mathrm{W/m^2/sr}] \tag{4}$$

The surface radiance is solved from this equation using the transmission coefficient and the path radiance as calculated by the MODTRAN model.

3.6. Apparent temperature

After the atmospheric correction from section 3.5, the resulting radiance is an estimation of the radiance originating from the scene. As stated above, this radiance consists of two components. The first component is the radiance due to emission from the objects (having a temperature above 0 K). The second component is the accumulation of all the reflections of the objects in the direction of the camera. If an object has a reflection coefficient that is zero and hence an emission component that is one, the estimated radiance is solely due to emission from the object. Consequently the temperature of the objects can be estimated using the integral of Planck's equation. If, however, the object is not a blackbody then a temperature can still be estimated. This estimated temperature is then most likely not the actual temperature of the object. It is referred to as *apparent temperature*. The relationship between the apparent temperature, T_{app}, and the radiance, I_{surf}, is given by the integration of Planck's equation:

$$I_{surf} = \int_{\lambda_1}^{\lambda_2} \frac{2hc^2}{\lambda^5} \frac{1}{e^{\frac{hc}{\lambda k T_{app}}} - 1} d\lambda \qquad [\mathrm{W/m^2/sr}], \tag{5}$$

with λ_1 and λ_2 are respectively the lower and upper bound of the wavelength of the MSIR. We use numerical inversion scheme for solving Eq.5. For a range of temperatures (with step 0.1 K), we first calculate the radiances, subsequently for an unknown radiance the two nearest points on the curve are determined and linear interpolation is used to estimate the temperature.

4. ANOMALY DETECTION

The purpose of anomaly detection is to locate and search for targets which are generally unknown, but relatively small with low probability of occurrence in the image. An anomaly detector extracts unknown targets which are thermally or spectrally distinct from their surroundings. In this work, we propose a method for anomaly detection, based on the analysis of their different thermodynamic behaviour with respect to that of the surrounding. We look for image blobs which are brighter (hotter) or darker (colder) than the surrounding, which periodic thermodynamic behaviour. Moreover, as we are looking for landmines, the shape of the image blobs will be used. This thermodynamic analysis is based on the principle of mathematical morphology (MM) [10]. This kind of processing allows detection of anomalies with certain size (or shape) and grey level characteristics. It is therefore much more advanced than simple thresholding, which only find the brightest or darkest objects in the scene.

The implement method follows roughly the work presented in [11], where the authors apply MM operators on spectral data taken at a specific time, whereas in the presented method multi-temporal and multi-spectral data is available. The flow diagram for the detector is depicted in Figure 4. The input is a set of multi temporal images. The detector is based on the assumption that there is a positive or negative contrast between the object and its background. After all the processing steps are performed, a binary mask is created that indicate the positions of the detected anomalies in the image set.

Three parameters are required for this algorithm. Two of them are related to the expected sizes of the anomalies, and one is used for histogram stretching. The following sections give summarize the different processing steps.

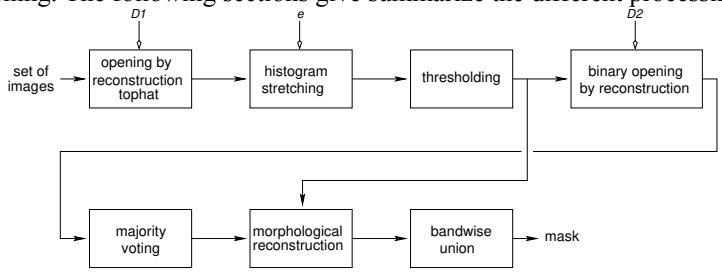

Figure 4: Flow diagram of the mathematical morphological detector.

4.1. Tophat filtering

The first and foremost step is the tophat filtering [12]. In this step, objects that are smaller than a certain size and brighter than their surrounding background are detected. This method uses a disk as a structuring element. The diameter, D_1, of the disk is chosen so that the largest expected objects can be detected. In our case it should be larger than the largest (expected) landmine. The image is filtered using the following equation:

$$t_i = f_i - r_B\left(f_i \circ D_1 \mid f_i\right),$$

where f_i is the input image (i=1..N, with N the number of images), t_i is the output (the filtered image), $r(\ )$ is the reconstruction function using B, a 3 by 3 structuring element, and $f \circ D_1$ is the morphological opening of image f.

Thermal diurnal images of buried objects are characterized by contrast change during time [3]. In fact, during natural heating, one can notice a smooth contrast change from bright to dark, or vice versa. In order to make use of this characteristic, for detecting anomalies, the so-called bottomhat filter is also applied to the diurnal mage sequence.

4.2. Histogram stretching and thresholding

To reduce the influence of outliers in the tophat/bottomhat-filtered images, histogram stretching is applied. This is done by finding the ε percentile lowest (I_1) and highest (I_2) values and re-scaling the image grey values to the interval defined by [I_1, I_2]. The resulting image is subsequently thresholded [14][15] at a value midway between the two calculated extremes.

The two extremes I_1 and I_2 are estimated using the following equations:

$$I_1 = \arg_I \left(C(I) == \varepsilon \right)$$
$$I_2 = \arg\max_I \left(C(I) == 1 - \varepsilon \right)$$,

with *C(I)* the normalised cumulative histogram and arg(*X*) the argument for which *X* is true. The intensity *I* is then mapped using the mapping function F_m:

$$F_m(I, I_1, I_2) = \begin{cases} 0 & \text{if} \quad I < I_1 \\ (I - I_1)/(I_2 - I_1) & \text{if} \quad I_1 \le I \le I_2 \\ 1 & \text{if} \quad I > I_2 \end{cases}.$$

The image is subsequently thresholded. In all our experiments the threshold has been fixed at 0.5.
The output G_i of this processing step is given by $G_i = T(F_m(t_i, I_1, I_2), 0.5)$, where *T* is the thresholding operator.

4.3. Binary opening

In order to remove the residual clutter (small image blobs) due to the image thresholding, a binary opening filter is applied. The structuring element is a disk with size D_2 such that $D_2 < D_1$ (otherwise all objects may be removed). The output O_i of this step, denoted as $O_i = R_B(G_i \circ D_2 \mid G_i)$, *R(.)* being the binary reconstruction using a 3 by 3 structuring element *B,* correspond to the bright/dark image blobs with a size lower than or equal to D_1.

4.4. Majority voting

Our objective is to detect image blobs (anomalies) with a constant behaviour (bright/dark) over time, i.e. blobs with the maximum occurrence of detection. For this, the results of the binary openings are summed, giving for each pixel the number of occurrences of an object at that location. The resulting image is then thresholded at level *l*, which is usually taken as half the number of images. The obtained binary image gives the locations of image blobs that are present in at least *l* images: $M = T\left(\sum_{i=1}^{N} O_i, l\right)$.

4.5. Morphological reconstruction

In order to recover the image blobs, in terms of size and shape, a morphological reconstruction operator, $L_i = R_B(M \mid G_i)$, is applied. It allows reconstructing the shape of the detected (located) image blobs, in M, from the images G_i.

4.6. Image Combination

The final step consists in combining the detection results L_i (i=1, …, N; N being the number of temporal images). This is done either by applying a binary OR operator, or by a summation over all the images, followed by a thresholding.

$$R = T\left(\sum_{i=1}^{N} L_i, \gamma \right)$$

with γ the selected threshold. The result of the anomaly detection process is shown in Figure 7.

5. IMAGE MOSAICS

Mosaics are generated for providing an overview of the surveyed area and locating the suspected objects on the ground. The mosaic generation procedure combines, following the scanning pattern, the 'ground projected' images. The mosaic can be seen as an aerial photograph. It allows geo-referencing the detected objects, since distances on the mosaic directly relate to distances on the ground. Although objects that have a height (like trees and vegetation) are distorted, we consider this mosaic to be more relevant than the panoramic view.

Following the survey characteristics of Section 2.2, the acquired images are ordered according to the scanning pattern (acquisition sequence). Moreover, for each acquired image we associate its line of sight, defined by the azimuth and elevation angles of the pan/tilt device, and the platform height, obtained from the recoded GPS information. The mosaic is obtained successively (following the scanning pattern) by applying to each acquired image the following procedure:

1. Map the current image onto the ground by back-projecting it (see Section 5.1)
2. Perform spatial image co-registration between the current ground projected view and the existing (from previous images) mosaic to correct for errors in position.
3. Insert the current ground projected view into the existing mosaic.
4. Perform histogram equalization to prevent changing in light conditions.

In the following sections each of these steps are explained in more detail.

5.1. Ground projection of images

The image acquired by the camera belongs to the 2D $I = \{(u,v)\} \in E^2$ image space, while the remapped image is defined as the $z = 0$ plane of the $W = \{(x,y,z)\} \in E^3$ 3D world space, considered as flat ground. Figure 5 shows the relationships between the two spaces W and I. The re-mapping process projects the acquired image onto the $z = 0$ plane of the 3D world space W.

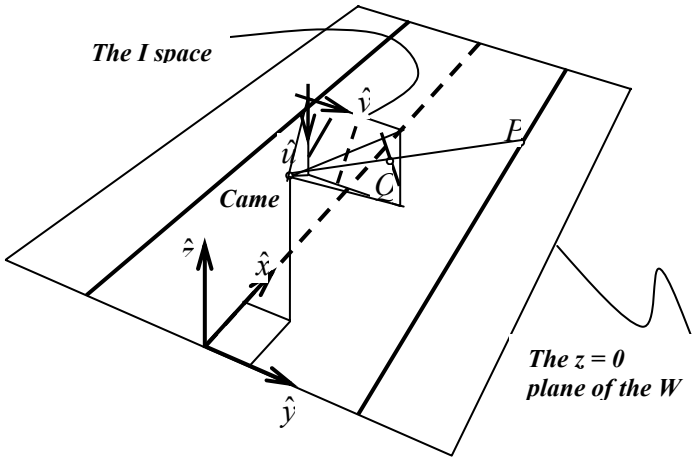

Figure 5: The relationship between the camera and word coordinate systems.

From Figure 5, the following parameters must be known in order to generate a 2D view of a 3D scene:

- *viewpoint*: the camera position is $C = (l,d,h) \in W$;
- *viewpoint direction*: the optical axis $\hat{o}$ is determined by the following angles:
  - $\overline{\gamma}$: the pan angle formed by the projection (defined by vector $\hat{\eta}$) of the optical axis $\hat{o}$ on the plane $z = 0$ and the x axis;
  - $\overline{\theta}$: the tilt angle formed by the optical axis $\hat{o}$ and vector $\hat{\eta}$;
- *aperture*: the camera angular aperture is 2α;
- *resolution:* the camera resolution is $n \times n$.

The transform $W \to I$ is given as follows:

$$u(x,y,0) = \frac{\operatorname{atan}\left[\frac{h \sin \gamma(x,y,0)}{\text{y-d}}\right] - (\overline{\theta} - \alpha)}{\frac{2\alpha}{n-1}}; v(x,y,0) = \frac{\operatorname{atan}\left[\frac{y-d}{x-l}\right] - (\overline{\gamma} - \alpha)}{\frac{2\alpha}{n-1}} \quad (6)$$

From Eq.6, one can notice the importance of the camera position, including original pan/tilt, and focal length. These parameters are obtained by using both geometric calibration of the acquisition system, at the start of the acquisition mission, and by using the GPS information, the azimuth and elevation angles during the scanning.

5.2. Spatial co-registration of images

The re-mapping process of Section 5.1 produces a ground projected view of the current image. It gives as well an estimate of where the current ground projected view should be placed within the mosaic. However, in order to correct for errors in placing the current ground projected view, mainly due to noisy height, azimuth and elevation angles parameters, a 'spatial' co-registration, between the already produced mosaic (obtained from previous images) and the current ground projected view, is applied. The Mutual Information based image co-registration procedure described in Section 3.2 is used to properly align the ground projected view of the current image with the existing mosaic, and hence produce a new (augmented) mosaic.

5.3. Histogram equalization

Due to changes in lighting conditions, during image acquisition, bright/dark image patches could appear in the produced image mosaic. Therefore, histogram equalization [16][17], using measurements from the overlapping areas between the previous mosaic and the current ground project view, is performed. The procedure is as follows:

1. Calculate the cumulative histograms C_m and C_i of the overlapping areas of the current mosaic and the overlapping areas of the current ground projected view, respectively
2. Find the optimal linear mapping, coefficients a and b, that minimises the differences between the cumulative histograms, $\sum_{g}\left[\boldsymbol{C_m}(\boldsymbol{g})-\boldsymbol{C_i}(\boldsymbol{a}\cdot\boldsymbol{g}+\boldsymbol{b})\right]^2$, g being the grey level values
3. Apply this mapping for the produced new mosaic image $I(x,y)$, $\boldsymbol{I_{hc}}(\boldsymbol{x},\boldsymbol{y})=\boldsymbol{a}\cdot\boldsymbol{I}(\boldsymbol{x},\boldsymbol{y})+\boldsymbol{b}$; $I_{hc}(x,y)$ being the corrected mosaic image.

Note that, the linear mapping is not perfect (in the sense that the histograms of the overlapping areas are not equal after transformation), but it allows mapping the higher and lower values of the non-overlapping areas of the mosaic to some meaningful values.

6. MINEFIELD TRIALS

With the support of BACTEC, end-user partner of the CLEARFAST project, the UNDP, the MAC Cyprus and the mine clearance organization ArmourGroup, we performed, during the period of November 15 2004 till November 30 2004, Minefield Trials in the United Nations (UN) Buffer Zone in Cyprus. Using the CLEARFAST demonstrator, described in Section 2 (Figure 1), a real minefield has been surveyed from different locations. According to the MACC's minefield records, the minefield contained a mixture of anti-personnel (AP) and anti-tank (AT) landmine. This has been also confirmed after the minefield clearance performed in December 2004 (some AT mines are visible in Figure 9).

Figure 6 shows, for one of the surveyed positions, thermal IR and visible mosaics covering an area of 20 m by 30 m. The area has been surveyed during 24 hours. A full scan (coverage) takes approximately 25 minutes, and hence 48 temporal scans have been acquired, each consisting of 261 images with approximately 30% overlapping. The calibration procedure, as described in Section 3, has been applied to the 12672 acquired images.

The temporal co-registration and the subsequent anomaly detection procedures, described in Sections 3.4 and Section 4, respectively, have been implemented to be applied to separate temporal field of views, i.e. diurnal images acquired with a given line of sight (given azimuth and elevation angles). Due to failings in the hydraulics of the (rented) sky lift, the temporal co-registration and anomaly detection have been applied to the 48 temporal mosaics of the full surveyed area (obtained using the procedure of Section 5). Because of the slow dropping in height and changes in the sky lift platform angles, during time, which induced a shift of more than 50% of the field of view of the images, temporal co-registration of separate field of views was impossible.

Figure 6, shows two selected regions of interests for illustrating the processing results, ROI A and ROI B, respectively. Figure 7 shows the detected anomalies within ROI A. For each detected anomaly, the estimated area, diameter, circularity measure, depth of burial, and thermal diffusivity (alpha) as estimated in [3], are given in Table 1. The circularity is estimated as the average between the ratio of the minor and major axis and the compactness.

Figure 8 and Table 2 illustrate the obtained results for ROI B. Figure 9 highlights the detected anomalies within the selected ROIs. It corresponds to a colour mosaic of an area of 8 m by 13 m.

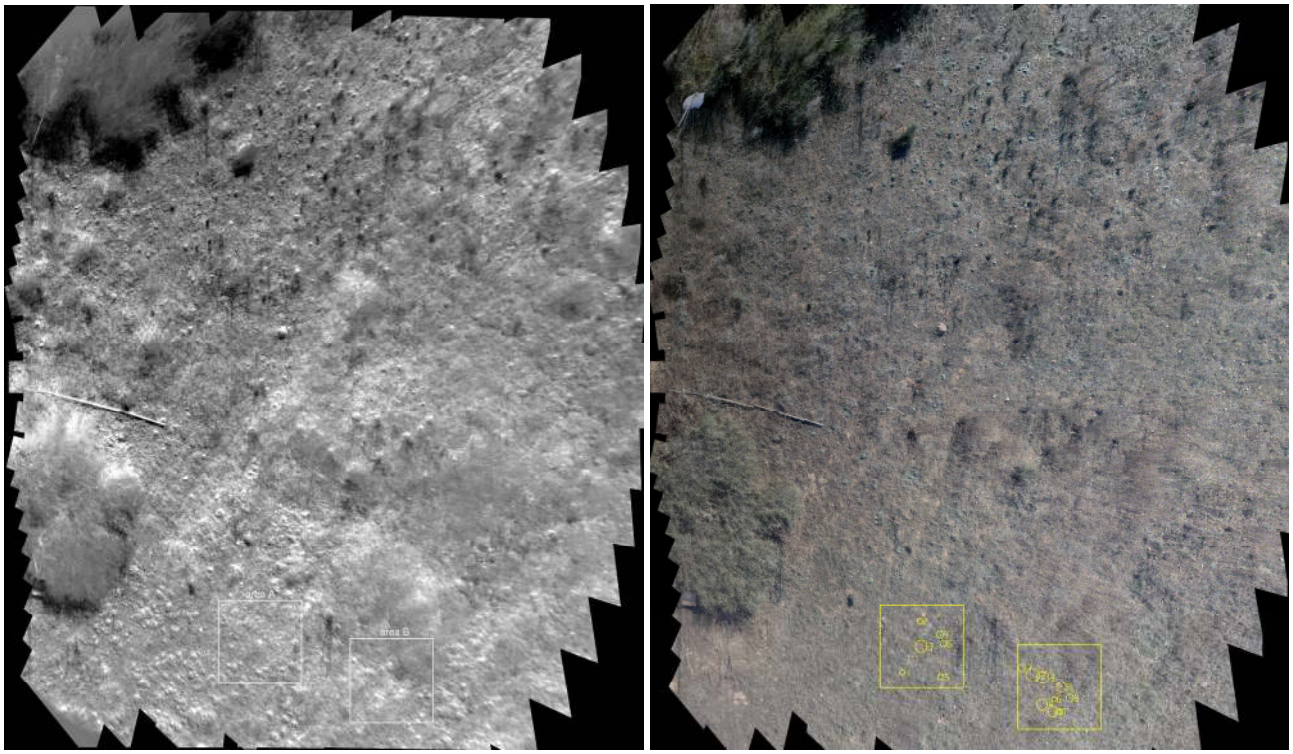

Figure 6: Mosaics of the surveyed 20 m x 30 m area, and selected ROIs for processing; Left: Thermal IR, Right: Colour image

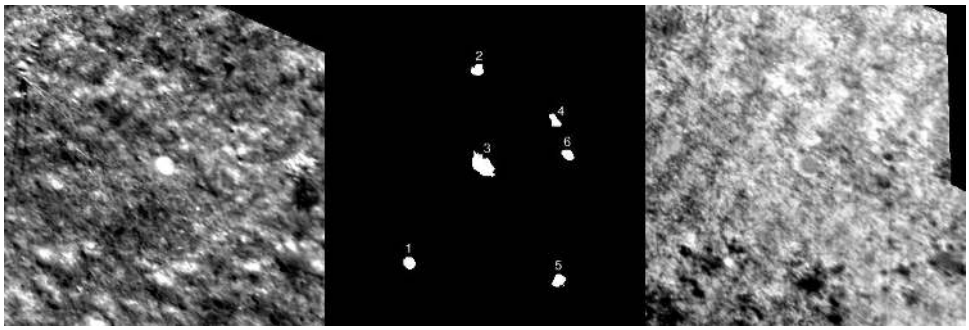

Figure 7 ROI A - Anomaly detection results; Left: mosaic IR at 09:58; Right: mosaic IR at 03:00; Middle: detected anomalies.

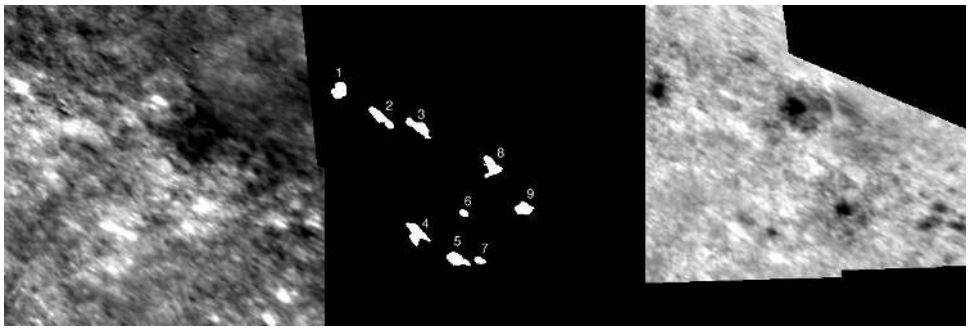

Figure 8 ROI B - Anomaly detection results; Left: mosaic IR at 09:59; Right: mosaic IR at 01:46; Middle: detected anomalies.

ID	X	Y	Area	Diameter	Depth	Alpha	Circularity
1	106	322	184	15.3	14	5.00E-08	0.908
2	191	81	181	15.2	5	3.50E-07	0.847
3	197	200	556	26.6	15	1.00E-06	0.567
4	287	144	149	13.8	15	5.00E-08	0.570
5	292	344	195	15.8	15	1.00E-06	0.823
6	304	187	156	14.1	6	2.00E-07	0.818

Table 1 Detected anomalies in ROI A

ID	X	Y	Area	Diameter	Depth	Alpha	Circularity
1	19	107	302	19.6	4	2.00E-07	0.790
2	70	141	338	20.7	15	1.00E-06	0.428
3	118	153	345	21.0	15	1.00E-06	0.422
4	115	285	416	23.0	15	1.50E-07	0.519
5	166	317	320	20.2	15	2.50E-07	0.571
6	174	260	86	10.5	15	1.00E-06	0.798
7	194	319	106	11.6	15	1.00E-06	0.723
8	209	202	356	21.3	15	1.00E-06	0.539
9	249	254	273	18.6	3	2.00E-07	0.780

Table 2 Detected in ROI B

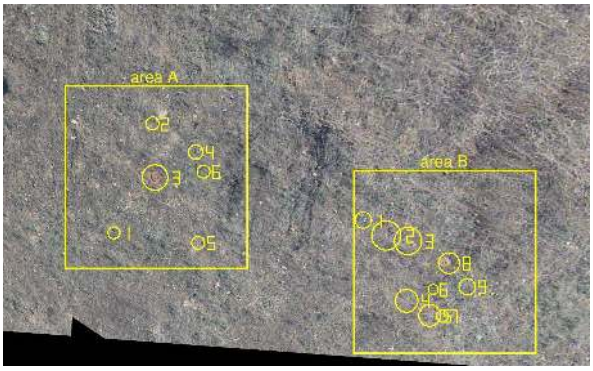

Figure 9 Colour mosaic with the detected anomalies in ROIs A & B.

The two visible AT mines of type M6A2 and diameter of 33.7 cm are marked as Object #3 in ROI A, and Object #8 in ROI B. From Table 1 and Table, they are circular in shape with a diameter of approximately 10% less than the expected one. The estimated depth of burial of 15 cm, indicated in Tables 1 and 2, corresponds to the maximum depth chosen for the estimation. This indicates that the algorithm did not succeed to estimate the depth of burial. This is explained by the fact the thermal model, described in [3], has been developed for buried objects. Moreover, the estimated thermal diffusivity, 1.00E-06, correspond to the initial value of the algorithm.

From the minefield records the AP mines are of type M2A4 and diameter of 10.4 cm. From Tables 1 and 2, and according to the estimated thermal diffusivity (alpha), the detected anomalies which are highly suspected of being AP mines are Object #6 in ROI A, and Object #1 and Object #9 in ROI B. The estimated objects diameter is in average 14 cm, the burial depth is in average 4 cm, and the thermal diffusivity approaching the diffusivity of TNT.

7. CONCLUSIONS AND DISCUSSION

This paper presented the CLEARFAST system concept and demonstrator. The developed demonstrator has been successfully deployed and operated in a humanitarian demining environment. Only minor (technical) problems occurred during the field trials. The image pre-processing steps were applied and assessed successfully on the acquired data. Due

to the problems with the sky lift, the planned processing chain had to be adapted and thus not all the acquired data has been processed yet. However, the full processing chain has been applied to one of the four surveyed locations. Temporal image mosaics with high quality have been produced. The proposed anomaly detection procedure performed on the selected regions of interest provided the detection of several suspected targets, among them the (visible) surface-laid anti-tank landmines. A number of detected anomalies with an estimated thermal diffusivity approaching TNT, may correspond to landmines that have been laid in close proximity to the AT landmines. The thermal diffusivity, as estimated using the thermal modelling in [3], is therefore an important cue for the target classification.

Though the deployment and operation of the demonstrator was successful, the full area needs to be processed to determine the system's performance by comparing the produced results and the ground truth we received from the MACC after clearance. This will be the subject of another paper.

ACKNOWLEDGEMENTS

This work has been partly funded by the European Commission, under the CLEARFAST project IST-2000-25173. The authors would like to thank the other project partners, namely, TAMAM, RLS, and BACTEC. TAMAM developed the pan/tilt, MSIR/visible cameras and data acquisition workstation. RLS developed the payload mounting, provided the RTK GPS and the dummy minefield. BACTEC developed the operational procedure concept and the methodology for assessing the results, selected the location, prepared and supported the execution of the Field Trial. Furthermore we would like to thank the UN (UMAS, UNDP), the MACC and Armour Group for their support and for giving us the opportunity to perform the field trial in Cyprus.

REFERENCES

1. J. MacDonald, J. R. Lockwood, et al., Alternatives for landmine detection. RAND Science and Technology Policy Institute, 2003, ISBN 0-8330-3301-8.
2. P. López, L. van Kempen, H. Sahli, D. C. Ferrer, *Improved Thermal Analysis of Buried Landmines*, IEEE Transaction on Geoscience and Remote Sensing, 4(9), pp. 1965 - 1975, 2004.
3. T.T. Nguyen, H. Dinh Nho, P. López, F. Cremer and H. Sahli, *Thermal Infrared Identification of buried landmines*, R.S. Harmon, J.T. Broach, J. H. Holoway, Jr. (Eds.), Proc. of SPIE 5794, Detection and Remediation Technologies X, Orlando (FL), Apr. 2005.
4. A. Irwin, J. Oleson and R. Robinson, *MIRAGE; Calibration radiometry system.* Proc. of SPIE 4027: Technologies for synthetic environment: hardware in the loop testing V, pp. 271-277, July 2000.
5. F. Cremer, Polarimetric infrared and sensor fusion for the detection of landmines, PhD thesis, Delft University of Technology, Delft, The Netherlands, 2003.
6. Gander, W. and W. Gautschi, *Adaptive Quadrature - Revisited*, BIT, Vol. 40, 2000, pp. 84-101. S. N. Toreres and J. E. Pezoa, Scene-based nonuniformity correction for focal plane arrays using the method of inverse covariance form. J. of Applied Optics, 42:29, pp. 5872-5881, October 2003.
7. B. Zitova and J. Flusser, *Image registration methods: a survey*, Image and Vision Computing, vol.21, pp. 977-1000, 2003.
8. H. Chen and P. K. Varshney, *Mutual Information Based CT-MR Brain Image Registration Using Generalized Partial Volume Joint Histogram Estimation*, IEEE Transactions on medical imaging, vol. 22, no.9, pp. 1111-1119, 2003.
9. A. Berk, L. S. Bernstein, G. P. Anderson, P. K. Acharya, D. C. Robertson, J. H. Chetwund, and S. M. Alder-Golden. *MODTRAN cloud and multiple scattering upgrades with application to AVIRIS.* Remote Sensing Environment, 65:367-375.
10. P. Soille, Morphological image analysis: principles and applications, Springer-Verlag, Berlin, 1999.
11. S. Batman and J. Goutsias, *Unsupervised iterative detection of land mines in highly cluttered environments.* In IEEE Transactions on Image Processing, Vol. 12, No. 5, pp. 509-523, May 2003.
12. F. Meyer*, Iterative image transformations for an automatic screening of cervical cancer.* J. Histochem. Cytochem., 27:128-135, 1979.
13. M. Sezgin and B. Sankur, *Survey over image thresholding techniques and quantitative performance evaluation.* J. of Electronic Imaging, 13:1, pp. 146-165, January 2004.
14. J. Kittler and J. Illingworth, *Minimum error thresholding.* Pattern recognition, 19:1, pp. 41-47, 1986.
15. J. Delon, *Midway image equalization.* Journal of Mathematical Imaging and Vision, Vol. 21, No 2, pp. 119-134, September 2004.
16. I. J. Cox, S. Roy, S. L. Hingorani, *Dynamic histogram warping of images pairs for constant image brightness.* IEEE Transaction on Image Processing, 1995